

Multifrequency Study of Giant Radio Pulses from the Crab Pulsar with the K5 VLBI Recording Terminal

Mikhail POPOV¹, Vladimir SOGLASNOV¹, Vladislav KONDRATIEV^{1,2,3}, Anna BILOUS^{1,4}, Olga MOSHKINA^{1,4}, Vasily ORESHKO⁵, Yury ILYASOV⁵, Mamoru SEKIDO⁶,
and

Tetsuro KONDO⁶

¹*Astro Space Center of Lebedev Physical Institute, Moscow, Russia*
mpopov@asc.rssi.ru, vsoglasn@asc.rssi.ru

²*West Virginia University, Department of Physics, Morgantown, USA*

³*National Radio Astronomy Observatory, USA*
vlad.kondratiev@gmail.com

⁴*Moscow Institute of Physics and Technology, Russia*
hanna.bilous@gmail.com, MoshkinaOlga@yandex.ru

⁵*Puschino Radio Astronomical Observatory, Puschino, Russia*
orshko@prao.ru, ilyasov@prao.ru

⁶*Kashima Space Research Center, NICT, Japan*
sekido@nict.go.jp, kondo@nict.go.jp

(Received $\langle \rangle$; accepted $\langle \rangle$)

Abstract

Simultaneous multifrequency observations of the Crab pulsar giant pulses (GPs) were performed with the 64-m Kalyazin radio telescope at four frequencies $\nu = 0.6, 1.4, 2.2$ and 8.3 GHz, using the K5 VLBI recording terminal. The K5 terminal provided continuous recording in 16 4-MHz wide frequency channels distributed over 4 frequency bands. Several thousand GPs were detected during about 6 hours of observations in two successive days in July 2005. Radio spectra of single GPs were analysed at separate frequencies and over the whole frequency range. These spectra manifest notable modulation over frequency ranges, $\Delta\nu$, both on large ($\Delta\nu/\nu \approx 0.5$) and small ($\Delta\nu/\nu \approx 0.01$) frequency scales. Cross-correlation analysis of GPs at 2.2 GHz showed that their pulse shapes can be interpreted as an ensemble of unresolved bursts grouped together at time scales of $\approx 1 \mu\text{s}$ being well-correlated over a 60-MHz band. The corresponding GP cross-correlation functions do not obey the predictions of the amplitude-modulated noise model of Rickett (1975), thus indicating that unresolved components represent a small number of elementary emitters.

Key words: Pulsars — giant pulses, Crab pulsar, PSR B0531+21 — e-VLBI

1. Introduction

Giant pulses (GPs) represent an extraordinary phenomenon in pulsar radio emission. First, they have huge peak flux densities, that may be as great as several millions of janskys (Cordes et al. 2004; Soglasnov 2006). Second, their duration is ultra short with GP fundamental components being even as short as < 2 ns (Hankins et al. 2003; Hankins & Eilek 2007). Third, these elementary nanopulses are strikingly almost completely circularly polarized, either left- or right-handed (Cognard et al. 1996; Popov et al. 2004; Hankins et al. 2003). Giant pulses are reliably known only from seven pulsars (see, e.g., Knight 2006, and references therein), but the properties of GPs were studied extensively only for two objects: for the original millisecond pulsar B1937+21 (Cognard et al. 1996; Kinkhabwala & Thorsett 2000; Soglasnov et al. 2004; Kondratiev et al. 2006), and for the Crab pulsar (see the most recent review by Bilous et al. 2008 and references therein). In contrast to regular radio pulses, which typically have Gaussian distribution, the cumulative distribution of GP energies follows a power law $N(E > E_0) \propto E_0^{-\alpha}$ with the exponent α being in the range of 1.5–2.5 (Popov & Stappers 2007; Bhat et al. 2008). These authors also reported about the deviation from the single power law fit of cumulative distributions at low energies. No deviations, however, were found at the highest energies even during 160-hours monitoring of the Crab pulsar with the Kalyazin 64-m radio telescope at frequencies of 0.6, 1.65 and 4.85 GHz (Popov et al. 2008). These three-frequency observations demonstrated that the pulse energy, in general, grows with decreasing frequency, and the spectral index is of about -1.8 . But radio spectra of individual giant pulses manifest deep modulations both at small and large frequency scales (Hankins & Eilek 2007; Popov & Stappers 2004; Popov et al. 2008). In this paper we present an analysis of results obtained from simultaneous 4-frequency observations of GPs from the Crab pulsar conducted with the 64-m Kalyazin radio telescope at the frequencies of 0.6, 1.4, 2.2, and 8.3 GHz using the K5 VLBI recording terminal. The description of the observing setup and data reduction pipeline is given in Section 2 and 3. The results of our GP studies at different frequencies are reported in Sections 4, 5, and 6, and the conclusions are given in Section 7.

2. Observations

Multifrequency observations of the Crab pulsar were conducted on July 20–21, 2005 with the 64-m Kalyazin radio telescope simultaneously at four frequency bands: 0.6, 1.4, 2.2, and 8.3 GHz. The total observing time was about 6 hours. The simultaneity of observations at four frequencies was possible owing to the multifrequency feed that the Kalyazin radio telescope is equipped with. To record the data we used the K5/VSSP VLBI recording terminal (Kondo

et al. 2002) and the K4 baseband converter provided by the Kashima VLBI group of the National Institute of Information and Communications Technology (NICT, Japan) for joint VLBI observations of pulsars under mutual agreement. The block diagram of the antenna feed line with the K5/VSSP VLBI recording terminal is presented in Figure 1. The terminal consists of 4 workstations with K5/VSSP PCI-bus boards, that allow to record up to 16 channels, each with the bandwidth of 4 MHz. The channels may be distributed in frequencies and/or polarizations by using the K4 baseband converter. In our observations we used the frequency setup presented in Table 1. the channel frequencies f_1-f_4 from the Table correspond to the lower edge of each frequency channel, and only upper sub-bands were recorded. At the frequency band of 600 MHz only one 4-MHz channel was used because of limitations by radio frequency interference. In all other bands we used four channels distributed along the whole band as indicated in Table 1.

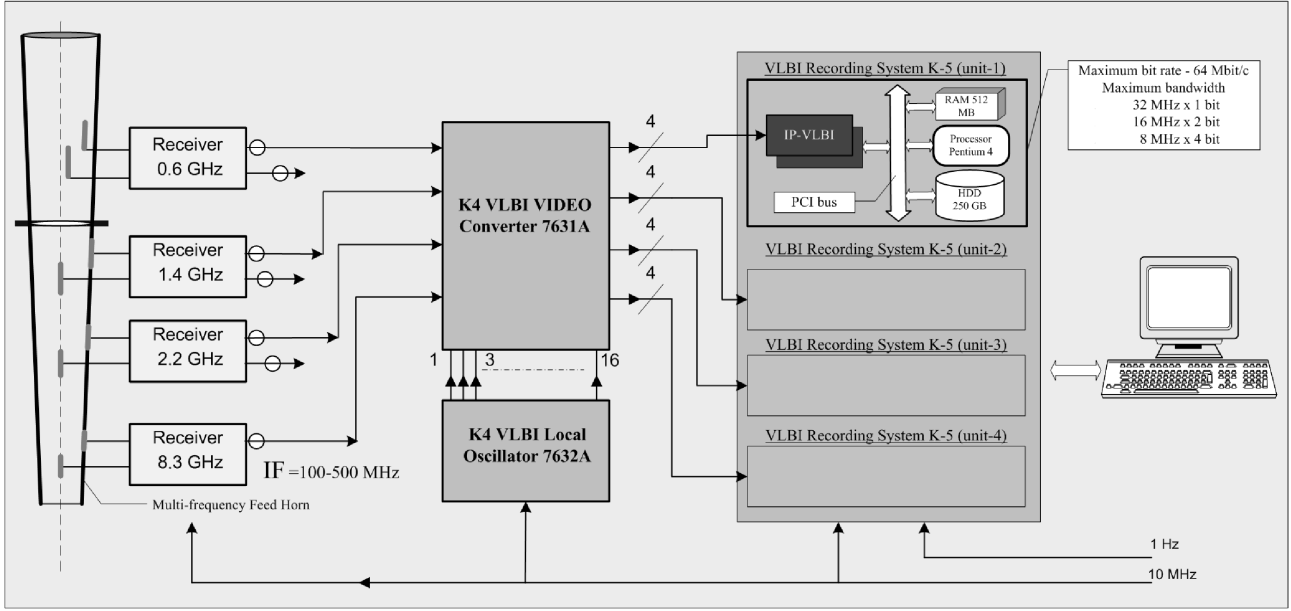


Fig. 1. Block diagram of antenna feed line of the 64-m Kalyazin radio telescope with the K5/VSSP VLBI recording terminal.

The system equivalent flux density (SEFD) for every band is dominated by the contribution from the Crab nebula and is given in the Table 1. Flux densities for the Crab nebula were calculated by using the relation $S_f = 955f^{-0.27}$, with f expressed in GHz (Cordes et al. 2004). At 8.3 GHz solid angle of the radio telescope beam covers only 20% of the area occupied by the nebula. Thus, we estimated the contribution from the Crab nebula to be 5 times less at this frequency assuming an uniform surface brightness distribution.

Table 1. Observations summary. Columns list the frequency band, the frequency channels setup for every band with the values corresponded to the lower edge of the channel, f_1 - f_4 , the system equivalent flux density (SEFD) including the contribution from the Crab nebula (see text), the estimated dispersion smearing time in a single frequency channel, τ_{DM} , the total number of events found in a total band, N_{p} , the peak flux density of the strongest event, S_{max} .

Band	Frequency channels (MHz)				SEFD (Jy)	τ_{DM} (μs)	N_{p}^*	S_{max} (MJy)
	f_1	f_2	f_3	f_4				
600	599.6	–	–	–	1300	8500	$\sim 10000^{**}$	2.2
1400	1395.0	1410.0	1425.0	1440.0	1150	650	1112	3.7
2200	2140.0	2160.0	2180.0	2200.0	1050	180	631	1.3
8300	8260.0	8280.0	8300.0	8320.0	240	3	1	0.04

* Giant pulses can be simultaneously detected in more than one frequency channel, i.e. the actual number of unique pulses detected is smaller than the total number of events in all frequency channels, N_{p} .

** See section 6 for explanation.

3. Data reduction

The core of the processing pipeline consisted of successive decoding of the data, correction for bit-statistics and dedispersion. Every single frequency channel was decoded according to the K5/VSSP (IP-VLBI) Board Data format¹ to produce the raw binary data stream. The decoded data represented the stream of only four alternating numbers: -3 , -1 , $+1$, and $+3$ according to the VLBA coding of 2-bit digitized values. These data were corrected then for the bit-statistics, i.e. the decoded values were adjusted to real ones that correspond to instantaneous $\pm 1\sigma$ brightness levels by using the technique developed by Jenet & Anderson (1998). To coherently dedisperse the data we used the predetection dispersion removal technique pioneered by Hankins (1971, see also Hankins & Rickett, 1975). More details about the correction for bit-statistics and coherent dedispersion can be found in Popov et al. (2002). However, for the coherent dedispersion, unlike the Eq. 1 from Popov et al. (2002), we have used the exact equations for phase correction:

$$\delta\phi(f) = \frac{2\pi\text{DM}}{Df} \left(\frac{\Delta f}{f_0} \right)^2,$$

where DM is the dispersion measure in pc cm^{-3} , $D = 2.41 \times 10^{-16} \text{ pc cm}^{-3} \text{ s}$ the dispersion constant, f_0 the lowest frequency of the frequency channel, f the current frequency, and $\Delta f = f - f_0$.

To allow for the direct comparison of times of arrival (TOA) of giant pulses, we reduced TOAs in all frequency channels within a band to the highest frequency (except for the data at 0.6 GHz where we had only one frequency channel). This was done by introducing a time

¹ http://www2.nict.go.jp/w/w114/stsi/K5/VSSP/data_format_e.pdf

delay via a linear phase correction k_f in the corresponding spectra simultaneously with the correction for $\delta\phi(f)$. The linear correction k_f is given by $k_f = 2\pi \times dt/N$, where dt is the time delay between corresponding frequencies in samples (including fractional part), and N is equal to the number of samples in the array used for the Fast Fourier Transform (FFT). We used $N = 2097152$, corresponding to the time interval of 262.144 ms and covering about 7.8 periods of the Crab pulsar. The dedispersion correction of every such chunk of data resulted in a number of spoiled samples in the restored signal due to the cycle nature of the convolution made through the FFT. The duration of this spoiled portion is equal to the dispersion time in a single frequency channel, τ_{DM} , of which the estimated approximate values are given in Table 1. To reconstruct the signal without gaps the successive chunks of data were overlapped by τ_{DM} . The used value of DM $56.738\text{cm}^{-3}\text{pc}$ was taken from the Jodrell Bank Crab Pulsar Monthly Ephemeris² (Lyne et al. 2008) for the epoch close to our observations.

To search for GPs at all frequencies except 600 MHz³, we set up the detection threshold at a level of 20σ above the mean value for the signal with the original sample time of 125 ns. The statistics of amplitudes x of such a signal is close to a χ^2 -distribution with 2 degrees of freedom $P(x > a) = \exp(-a)$, where P is the probability of the amplitude x of the signal exceeding the threshold a , and a is in units of σ . Thus, the probability of false detection with a threshold of 20σ above the mean level is 7.6×10^{-10} , and for the sampling rate of 8 MHz it will lead to a detection of one false GP in every 3 minutes. During the subsequent analysis only events that occurred in the narrow windows located at the longitudes of the main pulse and the interpulse were selected. These windows were each about $100\mu\text{s}$ wide and occupied only 0.6% of the period. Therefore, false detection happened only once per several hours.

The total number of detected events was about 10000, 2700, 1600, and 1 at the frequencies of 0.6, 1.4, 2.2, and 8.3 GHz, respectively (see Table 1). At 1.4 and 2.2 GHz sufficiently strong GPs were detected simultaneously in several frequency channels, and the number of real GPs is 2–3 times less than the total number of detections. The brightest GP was found at 1.4 GHz with the peak flux density of 3.7 MJy. Examples of strong giant pulses detected simultaneously at 1.4 and 2.2 GHz are shown in Figure 2.

4. Giant pulse at 8.3 GHz

Only one giant pulse was detected at the observing frequency of 8.3 GHz at a level of 30σ with a peak flux density of about 10 kJy, nearly equal in all four frequency channels. The pulse profile is shown in Figure 3. The event was not accompanied by notable emission at any of the lower frequency ranges, thus, proving $\Delta\nu/\nu \leq 0.5$ for the radio spectrum of this pulse. On the other hand, at 8.3 GHz the pulse flux density is constant over about 80 MHz. The only

² <http://www.jb.man.ac.uk/~pulsar/crab.html>

³ At 600 MHz we did not selected individual GPs (except for the preliminary search). Instead of this, we compared the overall statistical properties of signal on emission longitude windows with those on the noise.

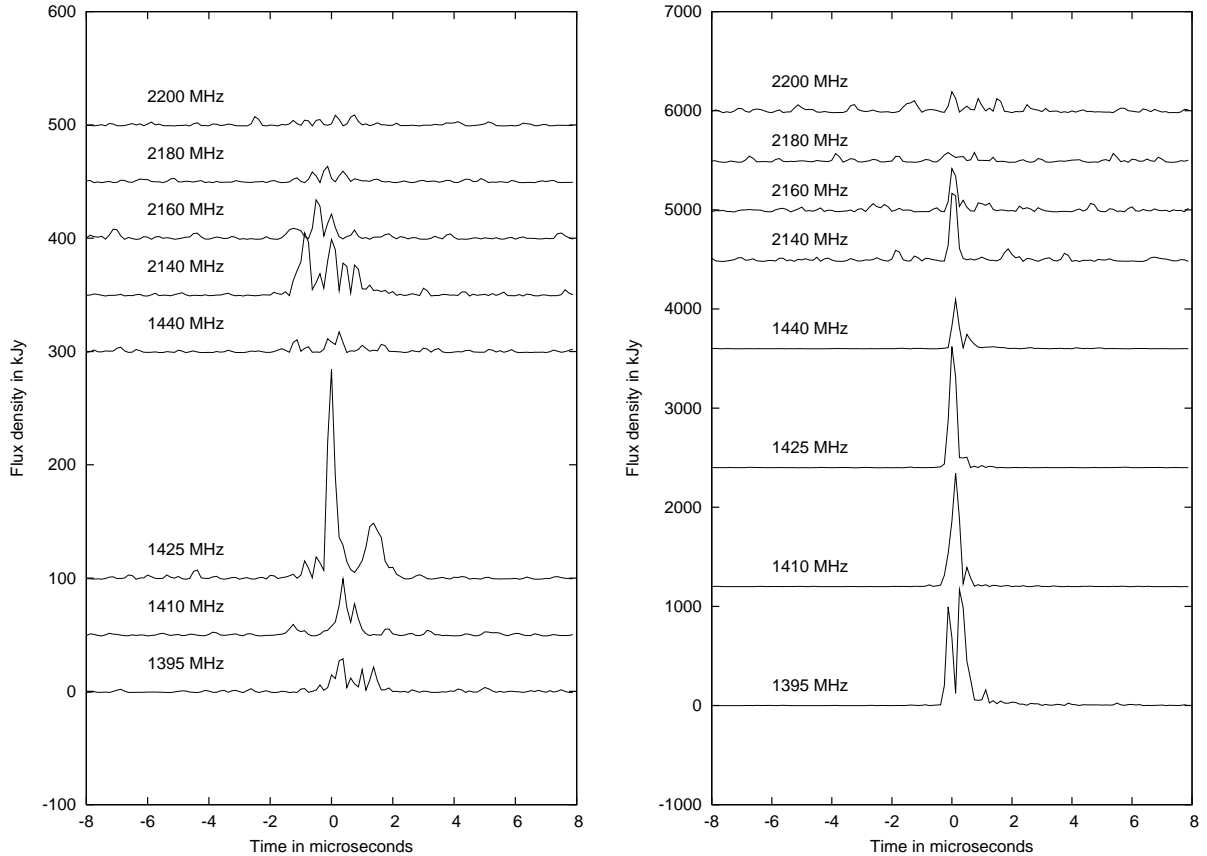


Fig. 2. Example of strong giant pulses detected simultaneously at 1.4 and 2.2 GHz in several frequency channels. The zero value in time corresponds to the sample with the maximum flux density of the giant pulse in any of the channels.

detection did not allow us to perform a statistical analysis of GP shapes, widths, and energies as we did for other frequencies (see below). High-frequency observations of giant pulses from the Crab pulsar were recently carried out by some of us with the 100-m Effelsberg radio telescope at 8.7, 15.1, 22.2 GHz. The first results from the ultra high time resolution data obtained with the Tektronix oscilloscope were reported by Jessner et al. (2008).

5. Giant pulses at 1.4 and 2.2 GHz

Unlike the high frequency of 8.3 GHz where only one GP was detected, we have found 1112 and 631 GP events in all four frequency channels at the frequency band of 1.4 and 2.2 GHz, respectively (see Table 1). Below we present a statistical analysis of GP energies and widths, and a study of radio spectra, shapes, and DM variation.

5.1. GP width and energy

Giant pulses vary significantly in their intensity and width, and show a broad variety in their shapes as can be seen in Figure 2. Therefore, it is rather difficult to compose an

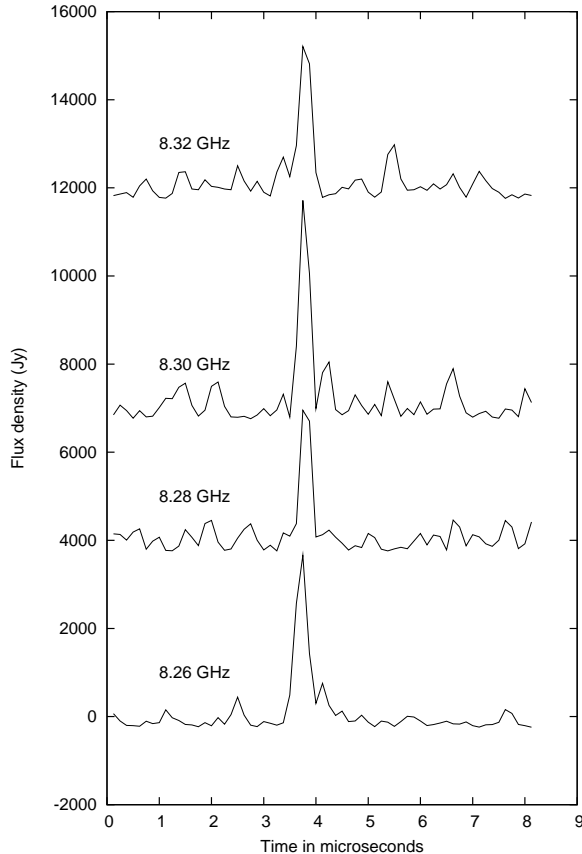


Fig. 3. Giant pulse detected at 8.3 GHz.

automated routine for GP’s shape analysis. In this paper we propose two different techniques for such an analysis: the first one is based on a calculation of an integrated flux density over varying time boxes in the vicinity of a given GP (this paragraph), and another method uses analysis of a signal variance (see paragraph 6.1.1). Let us define the total width of a giant pulse (w_{tot}) as a time interval Δt covering the vicinity of GP which contains 90% of the total integrated flux density of a given GP. We will calculate the integrated flux density (or pulse energy) as $E = \delta t (\sum_{i=0}^n (S_i - \langle S \rangle))$, where δt is sampling time (in our case $\delta t = 0.125 \mu s$), S_i are individual counts of reconstructed flux density. To exclude the noise contribution and calculate the “net” on-pulse energy, one has to subtract the mean off-pulse flux density, $\langle S \rangle$, computed for the off-pulse window from flux density value for every sample in on-pulse window where the required energy is calculated. In this paper we will express pulse energy in units of $\text{kJy } \mu s$. Following these definitions, we calculated, first, the maximum value for required pulse energy separated into two components E_0^+ and E_0^- as $E_0^+ = \delta t (\sum_{i=0}^n (S_{\max+i} - \langle S \rangle))$ and $E_0^- = \delta t (\sum_{i=0}^n (S_{\max-i} - \langle S \rangle))$. These quantities are calculated in the vicinity of a point of maximum flux density of a GP S_{\max} over n samples in positive and negative time directions. We use $n = 256$, corresponding to maximum expected

pulse width $\Delta t = 2n\delta t = 64\mu s$. E_0^+ and E_0^- may differ notably since pulse shape may be not symmetrical relative its maximum. With E_0^+ and E_0^- in hand we calculated trial values $E_k^+ = \delta t(\sum_{i=0}^k(S_{\max+i} - \langle S \rangle))$ and $E_k^- = \delta t(\sum_{i=0}^k(S_{\max-i} - \langle S \rangle))$ for every step k in organized loop from $k = 0$ to n . On every step k we compared the value of E_0^+ with the trial value of E_k^+ , and the value of E_0^- with the value of E_k^- . When the corresponding difference $|E_0^\pm - E_k^\pm|$ was less than $0.1E_0^\pm$, then the loop was terminated and corresponding time t^+ or t^- was determined as the edge of a GP. Thus, the total GP width w_{tot} was defined as $w_{\text{tot}} = t^+ - t^-$. Correspondingly, the GP energy E_p was defined as $E_p = E_k^+ + E_k^-$, and the effective width of GP as $w_e = E_p/S_{\max}$. Term w_e is traditionally used in pulsar researches, it describes time interval where most of pulse energy is concentrated, while w_{tot} corresponds to the whole pulse extent.

There is a strong constraint on the usage of this approach to analyse GP's shape. As it was already mentioned, the statistics of a detected signal in our case is close to a χ^2 -distribution with two degrees of freedom. For such a signal the root-mean-square deviation is equal to the mean value, i.e. the modulation index is equal to 1. Thus, the values of E_k^\pm will manifest notable fluctuations. To keep these fluctuations reasonably small one has to select only sufficiently strong pulses. We selected a threshold for the peak flux density for such pulses of 50σ for the estimated value for maximum pulse width of $w_{\max} = 64 \mu s$. Only 357 and 198 pulses met these requirements at 1.4 and 2.2 GHz, respectively.

Histograms of the total GP width w_{tot} at 1.4 and 2.2 GHz are shown in Figure 4 (left). Both top and bottom histograms are skewed heavily towards shorter total widths. Note that only very strong GPs were analysed; a weaker population of GPs may have a broader width distribution. Right histogram in Figure 4 represents the dependency between the maximum flux density, S_{\max} , and the effective pulse width w_e of a GP. It is clear that the strongest pulses tend to have shorter durations. The same tendency was found by Popov & Stappers (2007) at a frequency of 1.2 GHz on much broader statistics. We did not analyze the cumulative distributions at 1.4 and 2.2 GHz because of rather poor statistics as compared with the data used by Popov & Stappers (2007), but we will present such an analysis for our data, obtained at 600 MHz in section 6.

5.2. Instantaneous GP radio spectra

Given the multifrequency observations with the characteristic frequency setup (see Table 1) we were able to analyze instantaneous radio spectra of detected strong GPs both over large and short frequency scales. It is important to take into account the effect of interstellar scintillations when measuring the integrated flux density of a giant pulse in a given receiver band. For this we considered results of another experiment that was carried out by some of us over the course of our observations. This experiment was the two-station VLBI observations between the 64-m Kalyazin radio telescope and 43-m Algonquine radio telescope

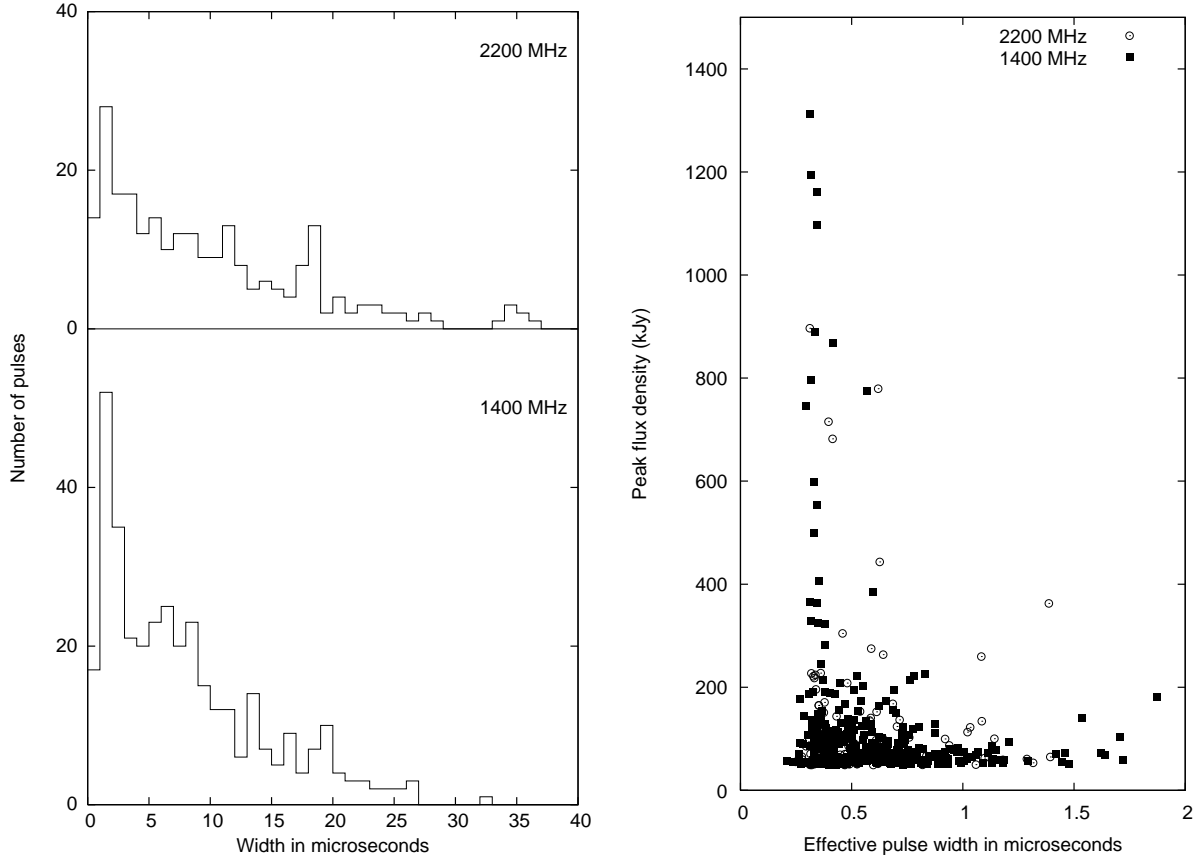


Fig. 4. Distribution of the total GP width w_{tot} (left), and dependence between the peak flux density S_{max} and the effective width of GP w_e (right) at 1.4 and 2.2 GHz.

(Canada) at 2244 MHz using the S2 recording system in a 16-MHz band (Kondratiev et al. 2007). In the cross-correlation functions (CCF) of radio spectra of GPs detected at two stations, two frequency scales of diffraction modulation of the spectrum at 2244 MHz were found to be 50 and 450 kHz with equal modulation indices (Kondratiev et al. 2007). Cordes et al. (2004) found that in the presence of interstellar scintillations the integrated flux density over the receiver band B will be subject to random fluctuations which follow a χ^2 -distribution with $0.4B/\Delta\nu_d$ degrees of freedom, where $\Delta\nu_d$ is the decorrelation bandwidth. In the case of $\Delta\nu_d > 0.2B$ the measured integrated flux density is fully modulated by diffractive interstellar scintillations. For the VLBI observations having $\Delta\nu_d = 450$ kHz at 2.2 GHz and $B = 4$ MHz, $\Delta\nu_d > 0.1B$ and the modulation of measured integrated flux densities will be still very significant. Following the steep power-law frequency dependence of decorrelation bandwidth $\Delta\nu_d$, $\Delta\nu_d \sim \nu^{4.4}$, for the Kolmogorov spectrum of electron density irregularities (see, e.g., Lorimer & Kramer, 2004), at a frequency of 1.4 GHz, $\Delta\nu_d$ will be about 5 times less than at 2.2 GHz, and the scintillation modulations will be considerably smoothed. Therefore, we analysed properties of instantaneous GP radio spectra at short frequency scales only for the frequency band of 1.4 GHz.

The left plot in Figure 5 shows an example of instantaneous GP radio spectra over 20

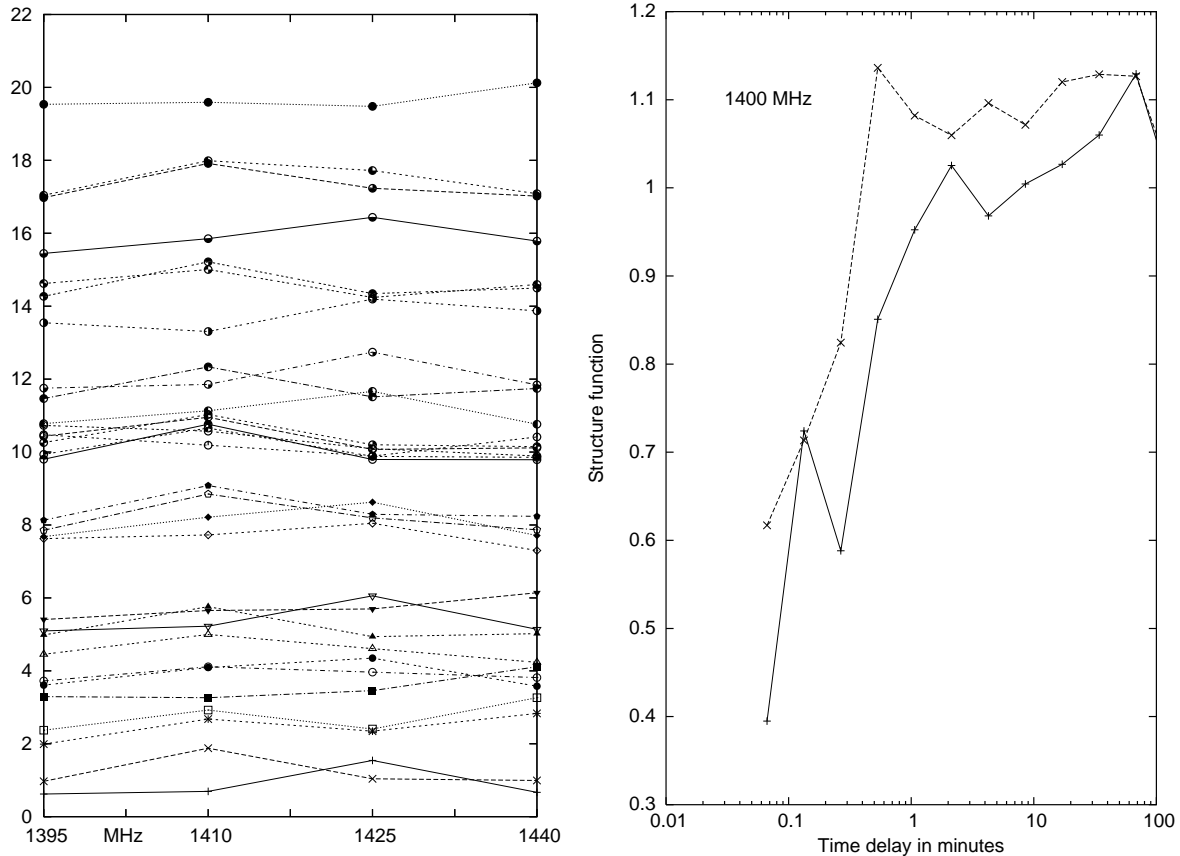


Fig. 5. Instant radio spectra of single GP (left) and their structure functions of time variations for two successive observing days (right) at 1.4 GHz. Every curve connecting the same symbols in the left figure represent the form of instant radio spectrum of a given GP. The location (shift) of a given spectrum at ordinate axis corresponds to the arrival time of the GP expressed in minutes from the beginning of the observing set.

minutes of observations at 1.4 GHz. Points presented by the same symbols and connected with the same type of a line represent the pulse energy measured for a given GP and expressed in arbitrary units, but with the same scale for an every curve. The every curve is placed at the ordinate axis in rough correspondance with arrival time of a given GP. Arrival time is expressed in minutes from the beginning of a selected observing interval. The whole figure corresponds to one continuum observing set. The variations of presented radio spectra with time seem to be random, but one can see that around the 10th minute of observations there are four GP spectra similar in appearance. This fact means that interstellar scintillations do still affect the measurements. To make a quantitative analysis we calculated a structure function $C^2(\tau)$ of time variations of instantaneous GP. A structure function is traditionally used in order to classify time variations of some quantity $Z(t)$ being investigated. For such a case $C^2(\tau) = \frac{1}{N} \sum_{i=1}^N (Z_i - Z_{i+\tau})^2$. Then, $C^2(\tau) = 0$ with $\tau = 0$, and $C^2(\tau) = \sigma^2$ for $\tau > t$ with t indicating a characteristic time of a variability of $Z(t)$. Here we transform the definition of $C^2(\tau)$ to apply it for the analysis

of time variations of 4-point instantaneous spectra Y_i^f as $C^2(\tau) = \frac{1}{M} \sum_{i=1}^N \sum_{f=1}^4 (Y_i^f - Y_{i+\tau}^f)^2$. Here, M is the number of combinations of radio GP spectra obtained within a given interval of time delay τ , N is the total number of GPs in this test, and $f = 1-4$ corresponds to one of four frequency channels listed in Table 1. The calculated structure functions, $C^2(\tau)$, for two successive observing days are shown in the right plot of Figure 5. It is evident that the structure functions got saturated at time intervals greater than one minute and decrease rapidly at shorter time delays. Thus, we do observe the effect of interstellar scintillations at 1.4 GHz that affects our measurements of radio GP spectra. Nevertheless, even at the shortest time delay (less than 10 seconds) between instantaneous GP spectra the structure functions still have a notable value of about 0.5 that can be due to an intrinsic modulation of GP spectra at a short frequency scale of $\Delta\nu/\nu \approx 0.01$.

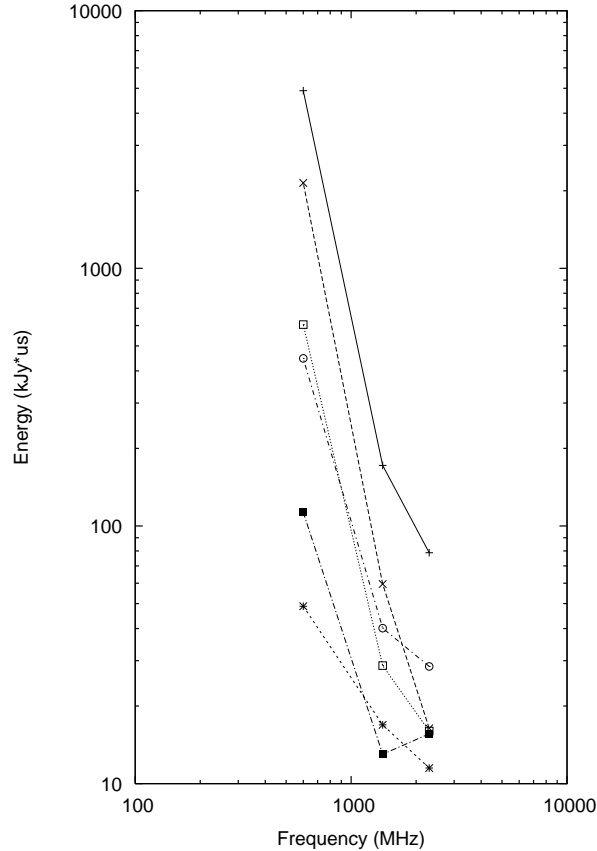


Fig. 6. Instantaneous radio spectra of single GPs in the frequency range of 0.6–2.2 GHz. Every polygonal line connecting the same symbols represents the spectrum of a selected giant pulse.

Examples of instantaneous radio spectra in the frequency range of 0.6–2.2 GHz for several GPs are presented in Figure 6. Every polygonal line connecting the same symbols represents the spectrum of a selected giant pulse. GP energies at 1.4 and 2.2 GHz were averaged over four frequency channels. There were only 27 strong GPs that occurred at all three observing

frequencies of 0.6, 1.4, and 2.2 GHz. The mean spectral index α is equal to -2.6 and -1.8 for 0.6–1.4 GHz and 1.4–2.2 GHz, respectively⁴ Though our estimates are based on poor statistics of GPs, the tendency for the spectral index α to flatten at higher frequencies is doubtlessly apparent. The same behaviour was reported by Popov et al. (2008) for a frequency range of 600–1650–4850 MHz.

5.3. DM variations

There are 952 GPs out of the total amount of 1112 GP events (or about 85%) found at 1.4 GHz that were identified with the GPs detected at 600 MHz. Therefore, we used them to determine the accurate values of DM by comparing their TOAs at two observing frequencies. The results are shown in Figure 7.

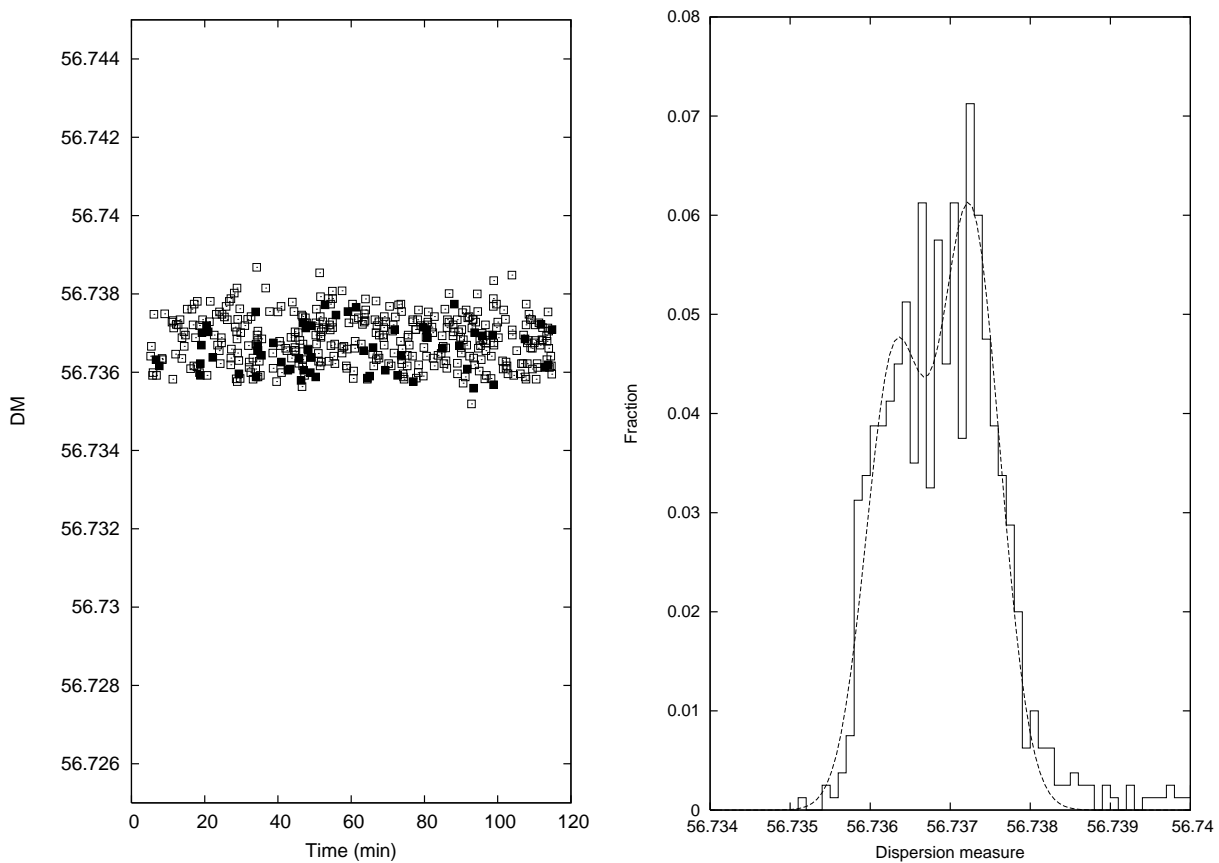


Fig. 7. Dispersion measure (DM) variations determined from times of arrival (TOA) of GPs at 600 and 1400 MHz. The left plot shows the measured DM values for different GPs versus the TOA of the giant pulse. Open squares show GPs that occurred at the longitude of the main pulse, while filled squares are those that occurred at the longitude of the interpulse. The right plot shows the histogram of DM variations. The dashed line is the two-Gaussian-component fit with the mean values of 56.7363 and 56.7373 pc cm^{-3} . This difference corresponds to the time shift of about 10 μs at 600 MHz.

⁴ The spectral index α is defined here as $E_\nu \propto \nu^\alpha$, where E_ν is the integrated flux density at frequency ν .

The left plot of Figure 7 represents the dependence of the measured value of DM of GPs versus their time of arrival. Hankins & Eilek (2007) pointed out that at high radio frequencies (above 4 GHz) DM values of GPs occurring at the longitudes of the interpulse, differ noticeably from DM values of GPs from the longitude of the main pulse. It is clear that in our observations at lower frequencies of 0.6 and 1.4 GHz there is no difference between DMs for GPs from different longitudes (see Figure 7, left). The right plot of Figure 7 shows the histogram of the dispersion measures of GPs. One can notice that the DM distribution is likely bimodal and can be well-fitted by two Gaussians with mean values of 56.7363 and 56.7373 pc cm⁻³. The difference $\Delta DM = 0.001 \pm 0.0001$ is estimated with a good formal accuracy. The difference corresponds to the time shift of about 10 μ s at the observing frequency of 600 MHz. As it follows from the left plot in Figure 7 the splitting can not be attributed to GPs occurred at different longitudes (MP and IP).

5.4. GP profile shapes

As will be shown below in section 6.3 during our observations the scattering contribution was small, and this allowed us to perform the analysis of intrinsic shapes of GPs detected at the frequency of 2.2 GHz. Indeed, the expected scattering time τ_{scat} at this frequency was $\lesssim 200$ ns as extrapolated from the τ_{scat} at 600 MHz, which is less than our time resolution of 250 ns (doubled sampling interval).

To study the profiles of individual GPs at the frequency of 2.2 GHz we used the approach of calculating the autocorrelation functions (ACFs) of GP profiles, the technique traditionally used to study the properties of the microstructure in pulsar radio emission (Hankins 1972; Cordes & Hankins 1973; Cordes 1976b). However, to avoid the noise spike at zero lag of the ACFs which would mask the presence of any unresolved components in GP profiles, we calculated CCFs between the profiles of the same GP recorded in different frequency channels. The cross-correlation function $R_{1,2}(\tau)$ between the profiles $I_1(t)$ and $I_2(t)$ of the same GP detected in two frequency channels is defined as

$$R_{1,2}(\tau) = [R_{1,1}(0)R_{2,2}(0)]^{-1/2} \sum_{t=1}^N I_1(t)I_2(t+\tau) ,$$

where t is the time sample within the GP, N is the total ON-pulse number of samples, and $I_1(t)$, $I_2(t)$ represent ON-pulse intensities with the OFF-pulse mean level subtracted. In our analysis we chose the duration of the ON-pulse window of 125 μ s, or $N = 1000$ samples. For our 4 frequency channels at 2.2 GHz there are $C_4^2 = 6$ different frequency combinations listed in the first column of Table 2.

Due to the effect of interstellar scintillations at this high frequency of 2.2 GHz many GPs were not sufficiently simultaneously strong in all frequency channels to provide a notable correlation coefficient for every pair of GP profiles. Thus, after the calculation of CCFs for all possible combinations of frequency channels for all 631 GP events found at 2.2 GHz, we chose only CCFs that have a sufficiently large value of correlation coefficient at zero lag. For an ACF

(or CCF) the root-mean-square deviation (σ_{acf}) near zero lag is equal to $\sigma_{\text{acf}} = 1/\sqrt{N}$. In our case for $N = 1000$, $\sigma_{\text{acf}} \approx 0.03$, and for the subsequent analysis we selected only the CCFs with the correlation coefficient at zero lag larger than $8\sigma_{\text{acf}} \approx 0.25$. There were 121 CCFs selected in this way.

Figure 8 shows an example of selected CCFs calculated for one of the strong GPs. One can see the notable correlation between all frequency channels. There are two apparent time scales in selected CCFs, namely a short one that occurred as a narrow feature that can be attributed to the presence of unresolved spikes in the GP structure, and an extended one with a duration of $\sim 1 \mu\text{s}$. The majority of the selected CCFs had the same appearance. To study the extended time scale feature, we smoothed the CCFs over 20 samples and selected only those with a correlation coefficient of 0.06 or larger at zero lag. Altogether, 102 of such CCFs were selected. The right plot of Figure 8 shows the distribution of both time scales (short and extended) measured at the half-level of the maximum of the corresponding broad feature. There is a broad jitter of widths of the extended scales in the CCFs from about $1 \mu\text{s}$ up to more than $2 \mu\text{s}$ with the mean value of about $1.3\text{--}1.4 \mu\text{s}$.

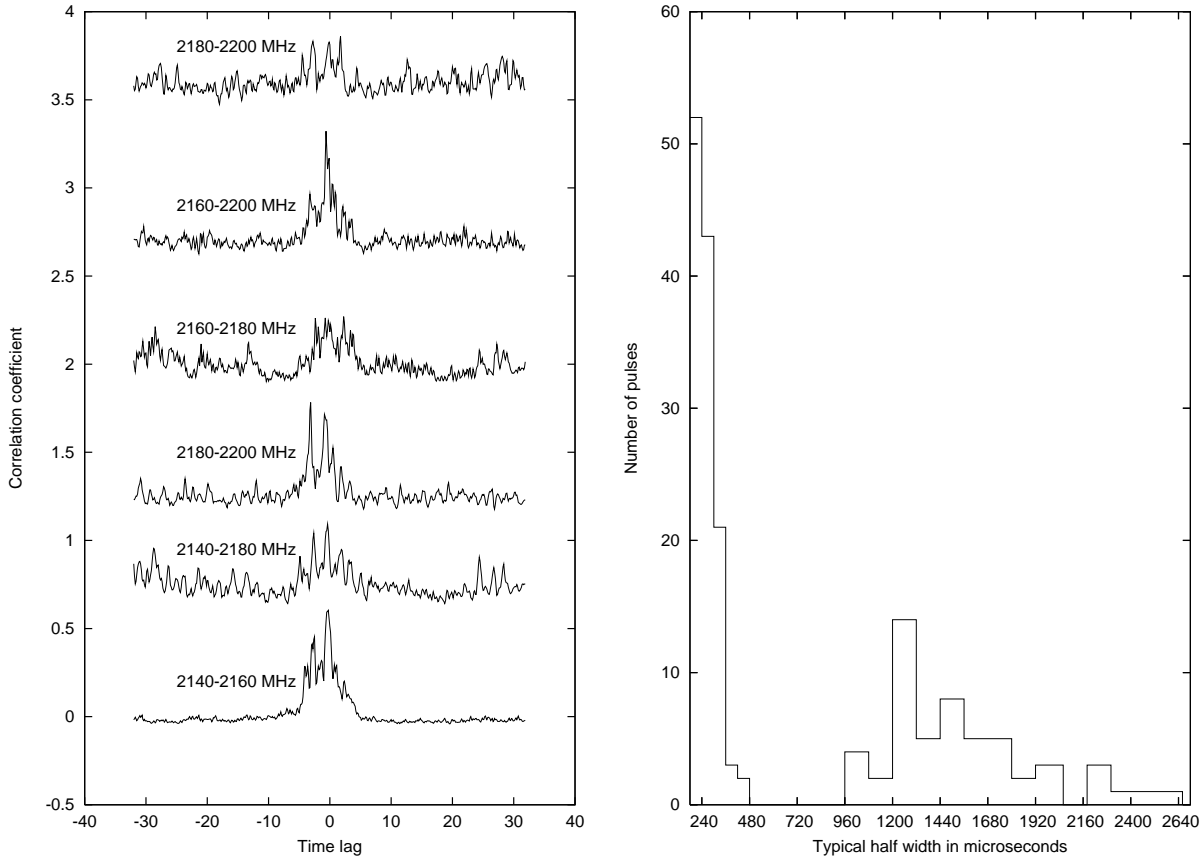


Fig. 8. Examples of cross-correlation functions (CCFs) between profiles in single frequency channels for one of the strong GPs at a frequency of 2.2 GHz (left), and the histogram of the half-widths of the two time scales detected in the CCFs (right).

Table 2. Extra non-dispersive time delay δt of the peak in the selected CCFs between GP profiles in different frequency channels. These delays represent the residual delays in time of arrival of GPs.

Frequency combination (MHz)	δt (μs)
2140–2160	-0.20 ± 0.04
2140–2180	-0.17 ± 0.04
2140–2200	-0.26 ± 0.07
2160–2180	0.05 ± 0.05
2160–2200	-0.06 ± 0.07
2180–2200	-0.01 ± 0.08

In addition to the measurements of the half-widths of the time scales detected in the CCFs, we also calculated the time delays of the CCF peaks relative to the expected value for the accepted DM. The results are listed in the Table 2. One can see that apparent deviations (at a level of $> 3\sigma$) in GP times of arrival are present only for the frequency channel of 2140 MHz (the lowest frequency channel at 2.2 GHz). These deviations measured in a 60-MHz frequency range (2140–2200 MHz) at 2.2 GHz are much smaller than the residual dispersion delays of about $2 \mu s$ found in arrival times of micropulses for the pulsars B0950+08 and B1133+16 at 1.65 GHz over a 16-MHz frequency range (Popov et al. 2002).

There is also another difference between CCFs computed for GPs in our current analysis and ACFs/CCFs calculated for the micropulses (see, e.g., Popov et al. 2002). Parameters of the microstructure are explained by the amplitude-modulated noise (AMN) model, developed by Rickett (1975). The model explains the pulsar microstructure as an envelope of a complex, white Gaussian noise process. Further elaboration of this model was done by Cordes (1976a) who postulated the origin of the shot noise as a coherent curvature radiation from bunched particles. Cordes (1976b) showed that ACFs/CCFs for micropulses do follow the prediction of the AMN model concerning the amplitude of the microstructure component in the average ACF/CCF. This amplitude is close to 0.5 at zero lag, when properly corrected for a signal-to-noise ratio (S/N) and for a time smoothing. Thus, even shortest micropulses do consist of a large number of such shots. However, the CCFs calculated for GPs in our analysis do not obey the prediction of the AMN model, and correlation coefficients at zero lag are often more than 0.5 level, even without the correction for the finite S/N (see Figure 8). Therefore, shortest GP components at 2.2 GHz consist of a small number of individual shots, or even a single elementary shot.

6. Giant pulses at 600 MHz

Giant pulses at 600 MHz appear more often than at higher frequencies. In more than 5 hours of observations we found 997 GPs with peak flux density greater than 30σ — 849 in main pulse and 148 in interpulse. The highest peak flux density detected was 2 MJy (1700σ).

Owing to unusually low scattering (see section 6.3), we were able to estimate the width of the pulses and find the energy distributions separately for pulses of different widths. Below we will briefly describe our calculation of energies and widths, and then discuss the results.

6.1. Data analysis

It is well known that GPs from Crab pulsar occur in two narrow longitude regions of about 6.7° each, called main pulse (MP) and interpulse (IP). Therefore, we analyzed data only from three relatively narrow windows: MP, IP and control noise window of the same size between MP and IP (with no pulsar emission).

At 600 MHz the search methods differed from those at other frequencies. Instead of selecting the pulses brighter than fixed threshold, we recorded the “width” and “energy” in all three windows on every period, regardless of the actual presence of giant pulse. The properties of GPs themselves were derived from comparison of the whole sets of “widths” and “energies” on MP/IP windows with those of the noise window. We believe such method has two main advantages. First of all, it allows us to neglect the unexpected deviations of noise from Gaussian. Second, it exempts us from selecting pulses by their peak flux density, which can be randomly biased by scattering. Considering all this, the analysis can be extended to weaker pulses.

6.1.1. Calculation of width and energy

Giant pulses have complex, jagged form, sometimes with several close components (see Figure 9). Here we considered another technique of GP’s width measurements compared with that proposed in paragraph 5.1. To find the width of GP, we used the fact that every giant pulse, regardless of its shape and peak flux density, is, in fact, a region with the increased variance of the signal S . Thus, on every MP/IP/noise window we computed a sequence of variances, σ_i^2 over small floating window:

$$\sigma_i^2 = \sum_{k=1}^N (S_{i+k} - \bar{S})^2$$

The size of the floating window, N , was comparable to the typical distance between the components (namely 200 samples, i.e. $25\mu s$). When such window covered GP, the variance rapidly increased. Since the size of the window was about the typical distance between the components of GP, the raise and decay were smooth and it was easy to measure the width of such outburst which we designated as $W_{\sigma_i^2}$. It was measured on the level of 5% of the peak maximum (see Figure 9). To obtain the width of GP (W_{GP}) we subtracted the size of the

window N from $W_{\sigma_i^2}$:

$$W_{GP} = W_{\sigma_i^2} - N .$$

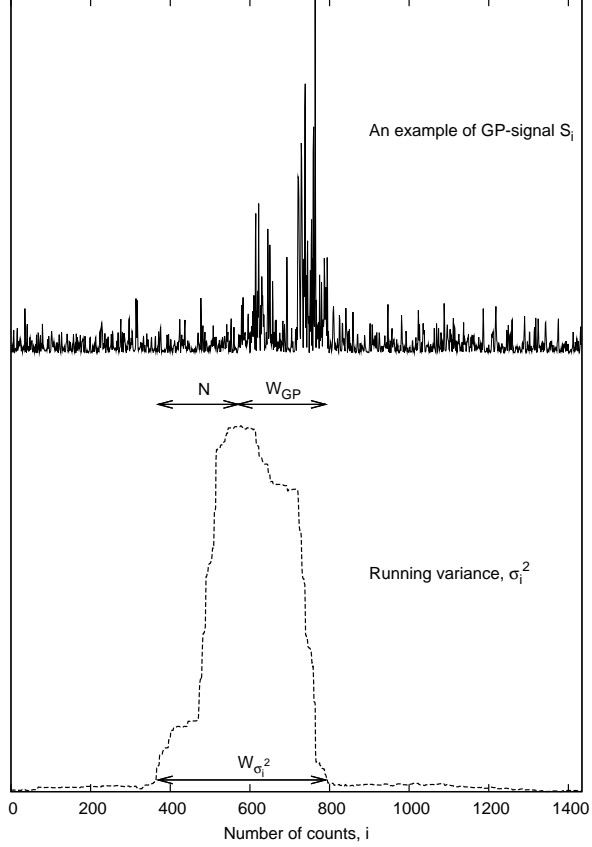


Fig. 9. Example of single pulse detected at 600 MHz, illustrating the technique of pulse width definition. Solid line represents the pulse intensity, and dash line shows the running variance. See text for more detailed explanation.

After that, the signal on corresponding MP/IP or noise window was smoothed with the value of the width. The maximum on the smoothed array was regarded as the total energy E_{tot} of an event, and obtained W_{GP} is understood as W_e . Then we converted derived W_e , expressed in samples, to microseconds with $\delta t = 0.125 \mu s$, and we scaled E_{tot} to $kJy \cdot \mu s$.

As was mentioned before, such procedure was performed in every period in three different longitude windows. On noise window $W_{\sigma_i^2}$ was usually less than the size of floating window N , resulting in negative “GP” widths. To unify the smoothing procedure we assigned all such negative widths the value of 1.

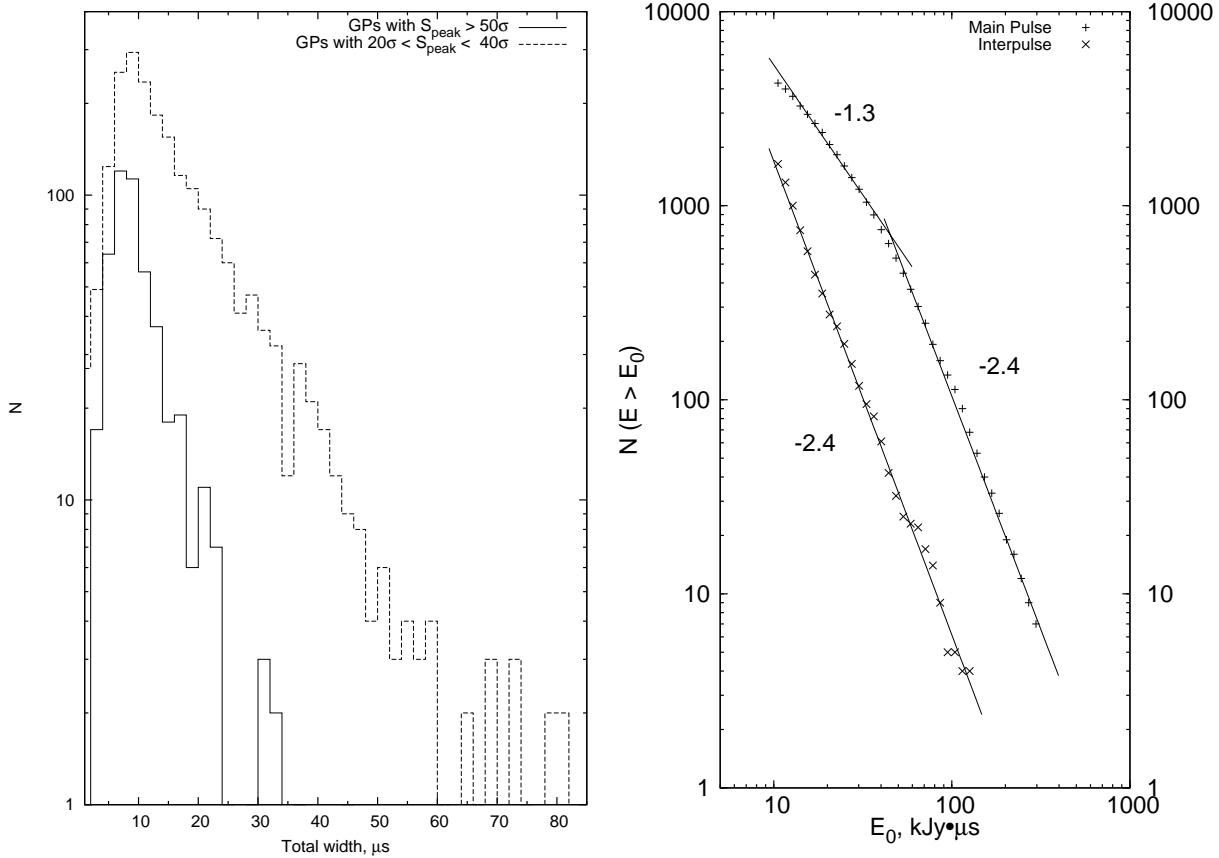


Fig. 10. Histogram of total widths (left), and cumulative energy distribution for GPs with widths of 16-24 μs at 600 MHz (right). Dash line in the histogram represents GPs with peak flux densities $S_{\text{peak}} > 50\sigma$ (the strongest GPs), while solid line is for weaker GPs.

6.2. GP widths and energies

As can be seen on Figure 10, the strongest pulses are, on average, narrow, and their width is comparable to the scattering width. The dimmer pulses are usually broader. The same tendency was observed at 1.2 GHz (see section 5).

The energy distributions for GPs both from the main pulse and the interpulse are well fitted by a power-law, with the indices depending on the range of widths selected (Table 3). However, for MP GPs wider than 8 μs , the energy distribution flattens at low energies (see Figure 10), while energy distribution for IP GPs of the same width and energy remains the same. Thus, the cumulative distribution for GPs from main pulse wider than 8 μs was fitted with 2 power-law functions:

$$N(E > E_0) = \begin{cases} E_0^{\alpha_1}, & E_0 < E_{\text{break}}; \\ E_0^{\alpha_2}, & E_0 > E_{\text{break}} \end{cases}$$

Such flattening was previously detected at other frequencies (Bhat et al. 2008; Popov & Stappers 2007 and references therein). The break energy for overall distribution, 35 $\text{kJy}\cdot\mu\text{s}$, is well consistent with the empiric formula for the break energy in dependence on the observed

Table 3. The power-law indices α of the cumulative energy distributions of GPs at the frequency of 600 MHz for different GP widths. Energies of GPs from the longitude of the main pulse have different power-law distributions for low-energy and high-energy GPs with the clear break energy E_{break} (see text) between them. We list both indices α_1 and α_2 for this case.

Total GP width, μs	Interpulse α	Main Pulse		$E_{\text{break}},$ $\text{Jy}\cdot\mu\text{s}$
		α_1	α_2	
< 8	-1.5	-1.4	-	-
8-16	-1.9	-1.2	-1.9	40
16-24	-2.4	-1.3	-2.4	45
> 24	-3.2	-1.0	-3.8	55
all	-2.0	-0.9	-2.2	35

frequency, derived by Popov & Stappers (2007):

$$E_{\text{break}} = 7\nu^{-3.4},$$

where E is in $\text{kJy}\cdot\mu\text{s}$ and ν in GHz.

6.3. GP scattering

At frequencies below ~ 1 GHz pulse shapes are dominated by the scattering broadening which decreases with increasing frequency for the Crab pulsar as $\tau_{\text{scat}} \propto f^{-3.5}$ (Popov et al. 2006a). However, the amount of scattering varies significantly with time. For example, Popov et al. (2006b) found τ_{scat} to be equal to $45 \mu\text{s}$ at the frequency of 600 MHz in their observations with the Kalyazin radio telescope in November, 2003. The measured value of τ_{scat} was estimated by fitting the exponential function $\exp(-t/\tau_{\text{scat}})$ to the tail of the average GP profile. In our current observations in July, 2005 the scattering broadening was 5–10 times smaller, and to approximate the average GP profile tail we used two exponents with the τ_{scat} of 4.5 and $17.5 \mu\text{s}$, with short-scale component being 4 times larger in amplitude. The mean GP profile was folded by summing 1436 GPs stronger than 50 kJy in peak flux density. They were preliminary averaged by 10 samples ($1.25 \mu\text{s}$), and aligned by their abrupt leading edges. The tail portion of the average GP profile at 0.6 GHz and its fit are presented in Figure 11. Smaller scattering contribution favoured our analysis of intrinsic shapes of GPs detected at 2.2 GHz (Section 5.4).

7. Conclusions

Accomplished study of giant pulses from the Crab pulsar from our simultaneous multifrequency observations with the Kalyazin radio telescope allowed us to draw a number of conclusions about the properties of Crab GPs:

1. Single GPs were often observed simultaneously in the three frequency bands of 0.6, 1.4, and 2.2 GHz, confirming the broad band nature of the GP emission. The spectral index α

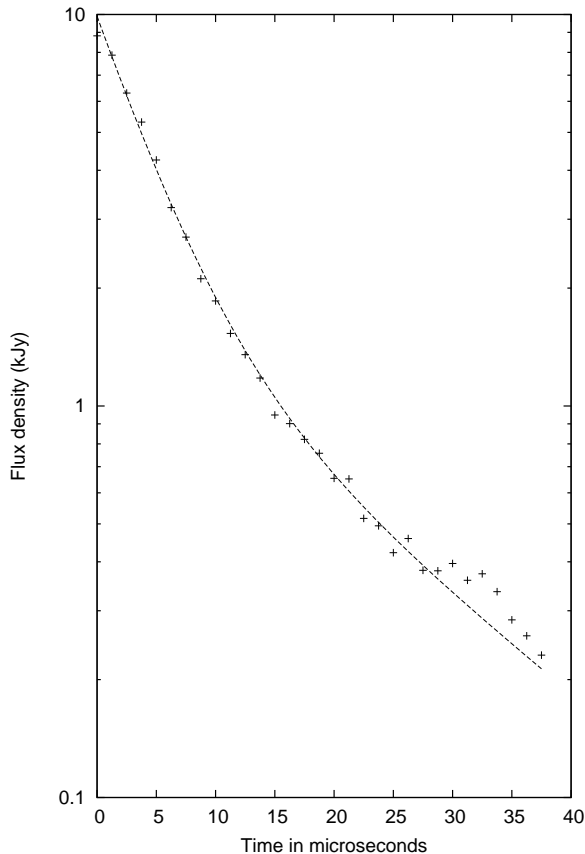


Fig. 11. The tail portion of the average GP profile at 600 MHz folded by summing 1436 GPs stronger than 50 kJy in peak flux density. The dashed line represents the fit by two exponentials $S = 8.1 \exp(-t/\tau_{\text{scat},1}) + 1.8 \exp(-t/\tau_{\text{scat},2})$ with the scattering times $\tau_{\text{scat},1} = 4.5 \mu\text{s}$ and $\tau_{\text{scat},2} = 17.5 \mu\text{s}$.

has a tendency to flatten towards higher frequencies ($\alpha_{0.6-1.4} = -2.6$ and $\alpha_{1.4-2.2} = -1.8$) as was also reported before by Popov et al. (2008).

2. Instant radio spectra of individual GPs do not follow the single power law in the frequency bands of 0.6, 1.4, and 2.2 GHz. Many GPs observed both at 0.6 and 2.2 GHz were not detected at 1.4 GHz, thus proving a notable spectra modulation at a frequency scale of $\Delta\nu/\nu \approx 0.5$. At the frequency of 1.4 GHz in addition to diffraction spectra distortions caused by the wave propagation through inhomogeneties of the interstellar plasma, we also distinguished the small-scale modulations in radio spectra at a level of $\Delta\nu/\nu \approx 0.01$ intrinsic to the pulsar.
3. GP profiles at the frequency of 2.2 GHz can be presented by unresolved spikes grouped together at a time scale of about $1 \mu\text{s}$. These unresolved components are well-correlated over 60-MHz bandwidth ($\Delta\nu/\nu \approx 0.03$). For comparison, Hankins (2000) did not find the correlation for the unresolved structure of GPs between 4535 and 4985 MHz (i.e., $\Delta\nu/\nu \approx 0.1$).
4. Cross-correlation functions of GP profiles in different frequency channels do not obey

the prediction of the AMN model (Rickett 1975) for the microstructure of the pulsar radio emission. Thus, unresolved components represent a small number or even the single elementary emitter.

5. The extra non-dispersive time delays of about $0.2 \mu\text{s}$ found in arrival times of unresolved components of GP structure at 2.2 GHz are not notable and 10 times smaller than the residual dispersion delays of about $2 \mu\text{s}$ found in TOAs of micropulses for the pulsars B0950+08 and B1133+16 at 1.65 GHz (Popov et al. 2002).
6. Strongest GPs tend to have shorter durations. Same results were reported by Popov & Stappers (2007) and by Bhat et al. (2008) at frequencies of 1.2–1.4 GHz.
7. The distribution of dispersion measures of GPs determined from their TOAs at 0.6 and 1.4 GHz is likely bimodal and can be well-fitted by two Gaussians with mean values of 56.7363 and 56.7373 pc cm^{-3} .
8. The cumulative distribution of GP energies at 600 MHz depends on the effective width of GPs. This distribution obtained only for GPs at the longitude of the main pulse, has the break and can be represented by two power-law functions with indices of $-2.0 - -0.9$ at high and low energies respectively. The value of the energy E_{break} , where this break occurred, is equal to $35 \text{ kJy} \cdot \mu\text{s}$, and it fits to the empiric formula $E_{\text{break}}(\text{kJy} \cdot \mu\text{s}) \approx 7\nu^{-3.4}$ with ν in GHz derived by Popov & Stappers (2007).

References

- Bhat, N.D.R., Tingay, S.J., & Knight H.S., 208, ApJ, 676, 1200
- Bilous, A.V., Kondratiev, V.I., Popov, M.V., & Soglasnov, V.A. 2008, in “40 Years of Pulsars: Millisecond Pulsars, Magnetars and More”, AIP Conf. Proc., 983, 118
- Cognard, I., Shrauner, J.A., Taylor, J.H., & Thorsett, S.E. 1996, ApJ, 457, L81
- Cordes, J.M. 1976a, ApJ, 210, 780
- Cordes, J.M. 1976b, ApJ, 208, 944
- Cordes, J. M., and Hankins, T. H. 1973, Bull. AAS, 5, 18
- Cordes, J.M., Bhat, N.D.R., Hankins, T.H., McLaughlin, M.A., & Kern, J. 2004, ApJ, 612, 375
- Kondo, T., Koyama, Y., Nakajima, J., Sekido, M., & Osaki, H. 2002, “Internet VLBI System based on the PC-VSSP (IP-VLBI) Board”, in IVS Symposium “New Technologies in VLBI”, held in Gyeongju, Korea on Nov 5–8, 2002
- Hankins, T.H. 1971, ApJ, 169, 487
- Hankins, T.H. 1972, ApJ, 177, L11
- Hankins, T.H. & Rickett, B.J. 1975, in “Methods in computational physics”, 14, 55
- Hankins, T. H. 2000 in Proceedings of IAU Colloquium 177 “Pulsar Astronomy – 2000 and beyond”, ed. Kramer, M., Wex, N. & Wielebinski, R (San Francisco: ASP), ASP Conf. Ser., 202, 165
- Hankins, T.H., Kern, J.C., Weatherall, J.C. & Eilek J.F. 2003, Nature, 422, 141
- Hankins, T.H. & Eilek J.F. 2007, ApJ, 670, 693
- Jenet, F. A., & Anderson, S. B. 1998, PASP, 110, 1467

- Jessner, A., Graham, D., Zensus, A., Popov, M.V., Soglasnov, V.A., Kondratiev, V.I., Bilous, A.V., & Moshkina, O.A. 2008, *A&A*, in preparation
- Kinkhabwala, A., & Thorsett, S. E. 2000, *ApJ*, 535, 365
- Knight, H.S. 2006, *Chin. J. Astron. Astrophys.*, 6, 2, 41
- Kondratiev, V.I., Popov, M.V., Soglasnov, V.A., et al. 2006, in Proc. of the 363rd WE-Heraeus Seminar, “Neutron Stars and Pulsars”, eds. W. Becker & H.H. Huang, MPE Report 291, 76
- Kondratiev, V.I., Popov, M.V., Soglasnov, V.A., et al. 2007, *A&AT*, 26, 585
- Kuzmin, A. 2006, in Proc. of the 363rd WE-Heraeus Seminar, “Neutron Stars and Pulsars”, eds. W. Becker & H.H. Huang, MPE Report 291, 72
- Lorimer, D. R., & Kramer, M. 2004, *Handbook of pulsar astronomy*, Cambridge University Press, 2004
- Lyne, A.G., Pritchard, R.S., & Graham-Smith, F. 1993, *MNRAS*, 265, 1003 (see <http://www.jb.man.ac.uk/~pulsar/crab.html>)
- Popov, M.V., Bartel, N., Cannon, W., et al. 2002, *A&A*, 396, 171
- Popov, M.V. & Stappers, B. 2004, *Astr. Rep.*, 47, 660
- Popov, M.V., Soglasnov, V.A., Kondratiev, V.I., & Kostyuk, S.V. 2004, *Astr. Lett.*, 30, 95
- Popov, M.V., Kuzmin, A.D., Ul’yanov, O.M., et al. 2006a, *Astr. Rep.*, 50, 562
- Popov, M.V., Soglasnov, V.A., Kondratiev, V.I., et al. 2006b, *Astr. Rep.*, 50, 55
- Popov, M.V. & Stappers, B. 2007, *A&A*, 470, 1003
- Popov, M.V., Soglasnov, V.A., Kondratiev, V.I., Bilous, A.V., Sazankov, S.V., Smirnov, A.I., Kanevskii, B.Z., Oreshko, V.V., & Ilyasov, Yu.P. 2008, *Astr. Rep.*, 52, 900
- Rickett, B.J. 1975, *ApJ*, 197, 185
- Soglasnov, V.A., Popov, M.V., Bartel, N., et al. 2004, *ApJ*, 616, 439
- Soglasnov, V. 2006, in Proc. of the 363rd WE-Heraeus Seminar, “Neutron Stars and Pulsars”, eds. W. Becker & H.H. Huang, MPE Report 291, 68